Single-Shot MeV Transmission Electron Microscopy with Picosecond Temporal Resolution

R. K. Li[*] and P. Musumeci

Department of Physics and Astronomy, UCLA, Los Angeles, California 90095, USA
(Received 13 May 2014; published 5 August 2014)

Pushing the limits in temporal resolution for transmission electron microscopy (TEM) requires a revolutionary change in the electron source technology. In this paper, we study the possibility of employing a radio-frequency photoinjector as the electron source for a time-resolved TEM. By raising the beam energy to the relativistic regime, we minimize the space-charge effects which otherwise limit the spatiotemporal resolution of the instrument. Analysis and optimization of the system taking into account the achievable beam brightness, electron flux on the sample, chromatic and spherical aberration of the electron optic system, and space-charge effects in image formation are presented and supported by detailed numerical modeling. The results demonstrate the feasibility of 10-nm–10-ps spatiotemporal resolution single-shot MeV TEM.

I. INTRODUCTION

Transmission electron microscopy (TEM) is an extremely powerful and versatile tool in many research areas, including biological, chemical, and material sciences, as well as for industrial applications [1–3]. For decades, one of the main efforts in improving TEM has been perfecting the spatial resolution. Recently, spherical and chromatic aberration correction modules have been successfully developed, and sub-Ångstrom spatial resolution has been demonstrated [4,5]. An actively ongoing trend in further extending the scope of the research that can be performed with TEM is to add the temporal dimension to the instrument capabilities, thus enabling real-time observation of microscopic dynamical processes [6–8]. Pioneering high temporal resolution TEMs based on modifying conventional commercial machines have been built and generated many appealing scientific results [9–15]. In order to overcome limitations related to beam brightness and *e-e* interaction-induced blurring to further push the boundaries in spatiotemporal resolution in electron-based imaging, a radically new approach to the electron source for TEM is needed. Here we discuss the design of a new generation of TEMs for ultrafast imaging.

One of the first successful attempts to develop a high-speed TEM at TU-Berlin produced an instrument capable of taking 10-ns temporal snapshots of the samples with a few hundred nanometers spatial resolution [9,10]. More recently, the dynamic transmission electron microscopy (DTEM) at Lawrence Livermore National Laboratory [11,12] demonstrated single-shot images of samples with 10-ns temporal resolution and 10-nm spatial resolution. At the relatively low energy (200 keV) of this instrument,

electron-electron (*e-e*) interactions in the lenses crossovers prevent the use of a beam current higher than a few mA and limit the spatiotemporal resolution. The ultrafast electron microscopy (UEM) technique developed at Caltech employs a different scheme—the stroboscopic method—using on average one electron per pulse to record images of reversible dynamic processes with approximately 500-fs temporal resolution [13–15]. Because single-electron packets have no space-charge broadening, the problem is eliminated at its roots, and the spatial resolution can approach a level similar to that achieved in conventional TEMs. On the other hand, millions or more electron pulses are needed to take each image with the repetition rate typically limited to the megahertz range to allow enough time for the sample to relax to its initial state. With this technique, one is restricted to dynamical processes occurring in the same exact way for each pump-probe cycle.

In this paper, we discuss the application of radio-frequency (rf) photoinjectors to single-shot picosecond temporal resolution MeV TEM. Among various types of high-brightness electron beam sources, photocathode rf guns have the unique capability of a very high acceleration gradient (approximately 100 MV/m), high final beam energy (approximately 3–5 MeV), and high beam charge (up to a few nC or 10^{10} particles per pulse) [16]. These sources have enabled the revolutionary advent of x-ray free-electron lasers (XFELs) [17] but have not been employed yet in electron-based imaging systems. Nevertheless, their potential for electron-scattering techniques is widely recognized, and the past decade has witnessed the exciting progress of using photocathode rf guns for ultrafast electron diffraction [18–24] and more recently for the initial exploration of time-resolved TEM [25–27].

In this paper, we consider various components of the system and present a complete feasibility study for a time-resolved MeV TEM capable of taking single-shot images

---
[*]Present address: SLAC National Accelerator Laboratory, Menlo Park, CA 94025, USA.

with 10-nm–10-ps spatiotemporal resolution, improving by 3 orders of magnitude on current state-of-the-art performances. In Sec. II, we analyze the requirements on beam quality and show the motivations behind the use of MeV beams for this application, independently of the particular design of the electron source and electron optics. In Sec. III, we present an optimization of the rf photoinjector beam to achieve transverse brightness and energy spread well beyond the state of the art, which fulfills the sample illumination requirements. In Sec. IV, we discuss the optical design of the column downstream of the sample and evaluate a scheme based on the use of quadrupole magnets as objective and projector lenses. This solution offers a convenient alternative to solenoidal round lenses, which quickly become large and expensive when the beam energy is scaled up to relativistic levels. In particular, we evaluate the aberrations and discuss the optimization of a permanent-magnet-based quadrupole triplet with effective focal length < 2 cm. Finally, in Sec. V, we consider the effects of e-e interactions including both smooth space-charge forces and stochastic scattering. With the help of self-consistent numerical modeling, we simulate the image formation process in the column for an idealized test sample. The results confirm the feasibility of capturing 10-nm resolution single-shot images by using 10-ps-long electron beams.

II. GENERAL CONSIDERATIONS FOR SINGLE-SHOT UEM

We begin our discussion with the estimate for the required electron flux to distinguish sample features having 50% contrast. Applying the Rose criterion [28] to evaluate the minimum number of particles to generate a clear signal above the noise induced by the Poisson statistics, we find the need for 100 or more electrons per spatial resolution unit d to maintain the shot noise below 10% and achieve a signal-to-noise ratio of 5. Therefore, roughly 4×10^6 electrons (0.6 pC) are required to form an image with 4×10^4 resolution units with an area of $200d \times 200d$. If we want to pack this amount of electrons in a single pulse with 10-ps bunch length, the peak current in the microscope column will be 60 mA or larger.

For these large peak currents, several orders of magnitude higher than those in conventional TEMs and 10–100 times larger than those in DTEM, there are a number of reasons to increase the electron energy to the MeV level. First, the higher electron energy significantly eases the issue related to stochastic Coulomb scattering. This effect cannot be compensated for by simply increasing the strength of the lenses, since random collisions essentially heat up the phase space. The effect of charged particle collisions in a crossover has been studied analytically by Jansen [29,30]. More recently, Reed and collaborators [31]] have analyzed numerically its consequences for time-resolved electron microscopy. By performing particle simulations for different beam energies with a pairwise model for e-e interactions, they find the blur on the final image to be negligible only provided the beam energy is above a few MeV.

Second, relativistic electron sources are typically characterized by very high extraction fields at the cathode, compared to conventional TEMs which are limited by arcing in the gun to gradients smaller than 10 MV/m [32]. The higher electric fields at the cathode allow one (for a given beam charge) to decrease the source size and improve beam brightness. Recent analysis shows that for an initial cigar aspect ratio (long and narrow pulse) a relatively large charge can be extracted from a small transverse region of the cathode. For example, more than 1-pC charge could be extracted from 10-μm spot size with a bunch length of 10 ps in the 100-MV/m peak field of an S-band photocathode rf gun [33].

Besides the challenging demand on the beam flux, small transverse emittance as well as very low energy spread are also critical to minimize the effects of spherical and chromatic aberrations and reach 10-nm spatial resolution. The required 6D phase space density greatly depends on the type of imaging mode that is planned for the microscope. For incoherent imaging, the resolution can be estimated by using

$$ d = \sqrt{(\lambda/\beta)^2 + (C_s\beta^3)^2 + (C_c\beta\delta\gamma/\gamma)^2}, \qquad (1) $$

where β is the objective aperture collection semiangle and $\delta\gamma/\gamma$ is the relative beam energy spread.

For simplicity, we can assume that the resolution is far above the diffraction limit (reasonable since for MeV electrons the de Broglie wavelength $\lambda < 1$ pm) and neglect the first term under the square root. It is then straightforward to obtain simple estimates for acceptable beam parameters from the spherical and chromatic aberration coefficients (C_s and C_c, respectively). These are related to the U_{1222} and T_{126} elements of the third- and second-order beam transfer matrices. As a first approximation, these have values comparable with the lens focal distance which for MeV electrons can be as short as 2 cm. It then follows from Eq. (1) that in order to get 10-nm spatial resolution we will need a relative energy spread lower than 10^{-4} and a collection semiangle $\lesssim 5$ mrad. Actually, in order to increase the contrast, it is preferable to have a smaller divergence, at most comparable with the Bragg angle, which is usually 1 mrad for MeV electrons.

Combined with the Rose criterion, we can use the beam divergence (equal to the collection angle in the bright-field imaging mode) as an upper bound to estimate the required transverse emittance. With a density of $100e/(10 \text{ nm})^2$ and a total charge of 0.6 pC, the rms spot size of the full beam at the sample must be smaller than 0.5 μm. Note that in this case the dose on the sample will be lower than the damage threshold [34]. As we push the spatial resolution to 1 nm

TABLE I.   Requirements on electron source parameters.

|	rf photogun	Picosecond MeV TEM
Number of electrons	10^7	$> 10^6$
rms normalized emittance	40 nm	< 10 nm
rms energy spread	10^{-3}	$< 10^{-4}$
FWHM bunch length	< 200 fs	10 ps

FIG. 1.   Comparison of 1.6-cell and 1.4-cell guns for (a) the output kinetic energy and energy spread (10-ps-long, low-charge electron beam) and (b) the acceleration gradient seen by the beam.

and beyond, dealing with the damage will become the limiting factor in the microscope design. In principle, if subpicosecond temporal resolution were to become feasible, one could attempt to use an ultrafast probe to outrun the damage by following the diffract-and-destroy scheme successfully demonstrated in XFELs [35].

For a $\gamma = 10$ beam with an rms beam divergence $\sigma_\theta = 1$ mrad, the rms normalized emittance is $\epsilon_n = 5$ nm. With these parameters, the coherence length of the beam $L_c = \lambda/2\pi\sigma_\theta$ is < 1 Å, so no coherent imaging will be possible. The initial operation mode of our single-shot picosecond MeV TEM is limited to incoherent mass-thickness contrast imaging. Other contrast mechanisms might be enabled by future improvements on the beam emittance using ultralow thermal emittance cathodes [36,37]. Substantial progress on the beam quality (in terms of both emittance and energy spread) will be required in order to enable single-shot high temporal resolution coherent imaging.

In Table I, we report the best performances of state-of-the-art rf guns [38,39] and the requirements for a 10-nm–10-ps imaging system validating the use of this source for time-resolved electron microscopy. One of the main challenges lies in the control of the energy spread. In the optimization discussed in the next section, we will trade off the bunch length to improve transverse emittance and energy spread enabling 10-nm spatial resolution imaging.

III. GENERATION OF THE ELECTRON BEAMS

Guided by the general considerations presented in the previous section, here we discuss the optimization of an rf photoinjector design aimed at generating electron beams suitable for single-shot picosecond TEM.

Because of the limits in the charge emission set by the initial charge density, the transverse beam brightness B_{4D} scales at least linearly with the extraction field E_0, the accelerating field at the cathode during emission [33,40]. For a pancake-beam aspect ratio we have $B_{4D} \propto E_0$, while for cigar beams the dependence is even stronger. In both cases, though, it is of paramount importance to maximize E_0. For this reason, we propose a 1.4-cell *S*-band photo-cathode rf gun structure instead of the more commonly used 1.6-cell type. The longer half-cell length was used in early designs to maximize the output energy and minimize the defocusing kick at the exit iris. This helped to control the emittance for 1-nC millimeter-size beams, but it is not
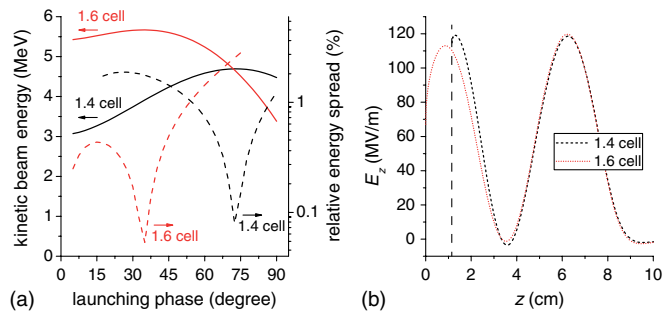
required for the much smaller beam sizes and charges needed for the microscopy application. On the contrary, by shortening the length of the first cell, the optimal injection phase (for maximum output energy and minimum energy spread) shifts from the typical 25°–35° range to around 70°–75° (see Fig. 1). The extraction field is thus increased by a factor of $\sin(70°)/\sin(30°) = 1.9$. For a gun operating at the 120-MV/m gradient, the extraction field will then be $E_0 > 110$ MV/m. The larger extraction field eases the space-charge effects at emission and in the propagation region close to the cathode, allowing very high current densities from a small area, minimizing the space-charge-induced emittance growth [40].

The small photoemission source area (a few tens of micrometers radius) is illuminated in our design by a long ultraviolet (UV) laser pulse to generate a cigar-aspect ratio electron beam. The initial transverse beam distribution is tailored to a spherical profile by properly shaping the UV laser pulse. If the initial longitudinal profile of the electron beam is parabolic, the beam will expand transversely driven by strong space-charge forces to form a nearly ideal uniformly filled ellipsoid. The final beam distribution is characterized by very linear phase spaces [38,41], and the beam emittance can be preserved close to its initial value [42–44]. As we will discuss in Sec. V, uniform charge density at the sample is required to maintain uniform space-charge defocusing along the beam. This uniformity can be achieved by employing a flat-top longitudinal profile. Since for very large aspect ratios the transverse and longitudinal dynamics are essentially uncoupled, space-charge forces cause a strong transverse expansion leaving the longitudinal profile essentially frozen. For the simulations in this paper, we use a 10-ps full width flat-top laser profile with fast-(100 fs) rising and falling edges. An initial emittance of 10 nm rad is obtained by assuming an intrinsic emittance of 0.5 mm mrad per millimeter rms initial spot size. This value for intrinsic emittance has been experimentally demonstrated [45] and can be further improved by lowering the UV photon energy to less than 0.1 eV above the effective cathode work function.
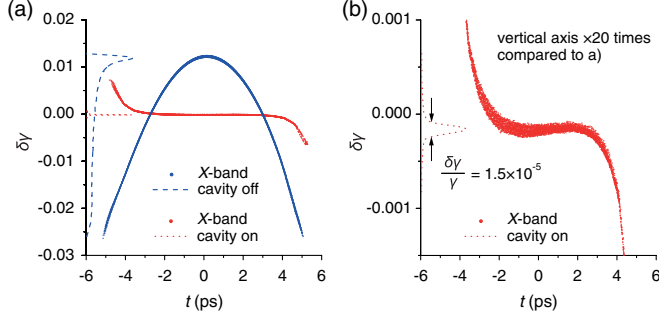
FIG. 2. (a) LPS of the beam before (blue dot) and after (red dot) the X-band cavity. The correlated energy spread $\delta\gamma/\gamma$ is reduced by 150 times. (b) LPS at the sample position. The vertical axis is zoomed in by 20 times compared to that of (a).

An important characteristic of such a long beam from an S-band rf gun is a relatively large energy spread. The longitudinal phase space (LPS) distribution at the gun exit has a strong rf curvature-induced correlation as shown in Fig. 2(a). The total beam energy spread is much larger than the uncorrelated width of the LPS distribution.

For a uniform 10-ps-long bunch (extending for $\Delta\phi = 10°$ of the S-band phase), we can calculate the rms energy spread at the gun exit from the expression for the output beam energy

$$\gamma_f = \gamma_0 \cos(\phi), \qquad (2)$$

where $\phi = 2\pi f_0 t$ is the output phase of the particles, γ_0 is the maximum energy, and $f_0 = 2.856$ GHz is the gun frequency [46]. We have $\gamma_0 = 10.19$ and $\delta\gamma_f/\gamma_f = 10^{-3}$, in good agreement with the General Particle Tracer (GPT) [47] simulation results in which space-charge effects are included, as shown in Fig. 2, and much larger than what is required for imaging application. This quantity is proportional to $\Delta\phi^2$; thus, in order to reduce it to an acceptable level, one possibility is to use a <1-ps-long beam at the cathode. But, in this case, the peak current would then be 10 times larger, resulting in unbearable space-charge effects and emittance degradation.

We analyze a different solution involving the use of an additional rf cavity as an energy spread compensator. At first order, the LPS distribution is characterized by an almost ideally quadratic curvature which can be compensated by using a higher harmonic rf cavity operating at the opposite deceleration phase. As an example, we consider the $f_1 = 4f_0 = 11.424$ GHz X-band cavity, and the final beam energy after the compensator cavity is

$$\gamma_c = \gamma_0 \cos(2\pi f_0 t) - \gamma_1 \cos(2\pi f_1 t), \qquad (3)$$

where γ_1 is the maximum energy gain of the X-band cavity. To cancel the quadratic term we need $\gamma_1 = \gamma_0/(f_1/f_0)^2 \approx$ 0.6. Such a small amount of energy loss can be realized by using a single-cell (length $L_X = 0.83$ cm) X-band cavity at

a few tens of MV/m gradient. The compensator cavity will be placed immediately following the S-band gun and before the condenser lens to minimize chromatic effects. A previously proposed two-frequency rf gun is a similar concept and might fulfill the beam requirement for single-shot picosecond TEM [48–51].

In Figs. 2(a) and 2(b), we show the compensated LPS (red dots), and the correlated beam energy spread $\delta\gamma/\gamma$ is reduced to a low 10^{-5} level (FW50 definition, full width containing 50% of the particles), in agreement with an analytical estimate of the residual energy spread from the higher-order terms in the rf curvature (proportional to $\Delta\phi^4$). Most of the final beam energy spread is due to residual longitudinal as well as transverse space-charge forces. We note that the success of the rf curvature compensation scheme relies on precise and high-stability control of the amplitudes and phases of the S-band and X-band rf sources, enabled by recent advances on rf-laser synchronization [52,53] and high-stability modulator technologies [54,55].

Once a beam with the correct phase space properties (energy spread and transverse emittance) is generated, the next component in the microscope is the transport optics required to illuminate the sample under optimal conditions. This function is typically performed by one or more condenser stages in a TEM. In this paper, we restrict the discussion to only a single-lens condenser stage instead of a more flexible multilens design [56] in order to minimize the number of beam waists (high charge density regions) in the system. A two-lens condenser stage could be considered for improving the flexibility of operation.

In Fig. 3(b), we show the evolution of the rms spot size σ_x and the normalized emittance ϵ_n from the cathode at $z = 0$ to the sample position at $z = 0.75$ m with the condenser lens tuned to deliver a beam waist at the sample position. A collimation aperture is located at 60 cm to block the particles with divergence larger than 2 mrad. The transverse density profile and trace space distribution at the sample plane are shown in Figs. 3(c1) and 3(c2). The sample area within a 2-μm-diameter circle is quasiuniformly illuminated by an average electron flux $200e/(10 \text{ nm})^2$, and the rms beam divergence is $\sigma_\theta = 1.0$ mrad with a quasiuniform x' distribution.

An optimized set of parameters of the electron source design and simulated beam parameters are reported in Table II. The improvements discussed in this section, including a shorter (1.4-cell) gun design, cigar aspect-ratio beam shaping, and a higher harmonic (X-band) cavity-based correlated energy spread compensation, show the feasibility for an rf photoinjector design to satisfy the beam illumination requirements for single-shot picosecond MeV TEM.

IV. DESIGN OF THE ELECTRON-OPTICAL COLUMN

The downstream section of the electron-optical column consists of several lenses that image the beam from the
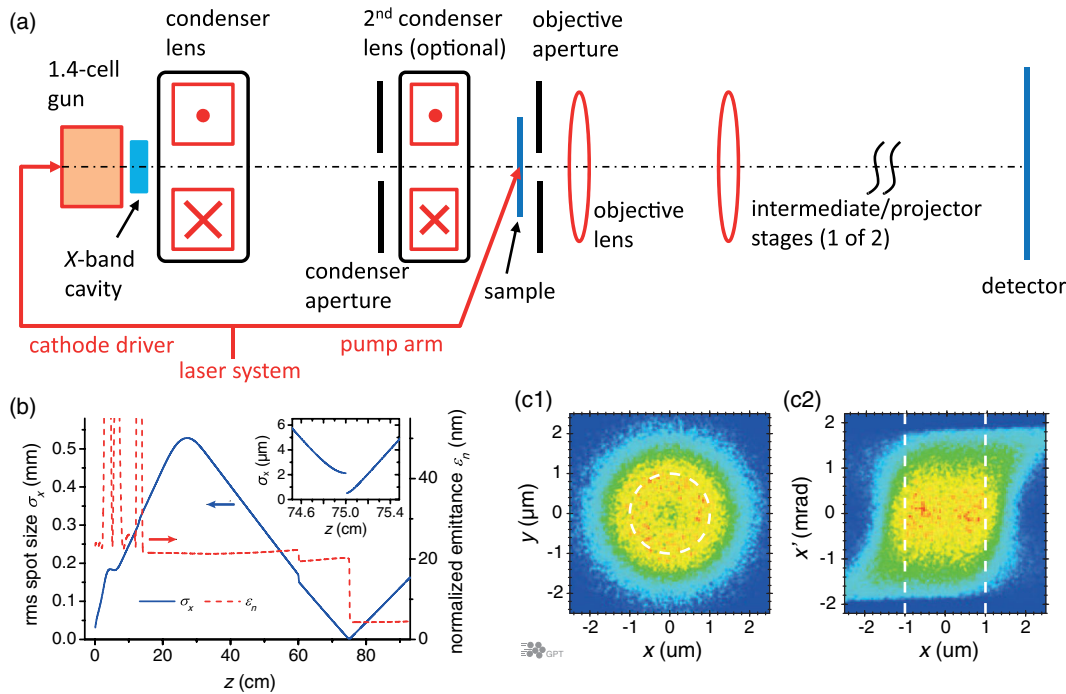
FIG. 3.   (a) Cartoon concept of the single-shot picosecond MeV TEM. (b) The rms spot size σ_x and normalized emittance ϵ_n along the beam line. The inset plot shows σ_x evolution close to the sample location at $z = 0.75$ m. (c1) The x-y profile and (c2) x-x' distribution of the electron beam at the sample position. Within a 2.0-μm-diameter area, indicated by white dashed lines, the beam has quasiuniform position and angular distributions.

sample (object plane) to the detector (image plane). In most TEMs, this section typically includes 3–6 stages, with an objective lens, one or more intermediate lenses, and one or more projector lenses. The spatial resolution of TEMs is strongly dependent on the optical properties of these lenses, in particular on the spherical aberration C_s and chromatic aberration C_c of the objective lens closest to the sample, where the beam divergence is largest. To minimize C_s and C_c and achieve high spatial resolution, generally very strong objective lenses are utilized [4,5]. Minimization of the objective focal length f is also important to obtain a

TABLE II.   Parameters for the operation of the electron source and the electron beam qualities at the sample.

Parameters	Values
Gun gradient	120 MV/m
Gun phase	73°
Initial beam charge	6.0 pC
UV spot size, rms (spherical)	20 μm
UV pulse duration, FWHM	10 ps
X-band cavity gradient	43.3 MV/m
At the sample (within the 2.0-μm-diameter area)	
Beam charge	1.0 pC
Transverse momentum spread $\gamma\sigma_\theta$, rms	9.5×10^{-3}
Bunch length, FWHM	10 ps
Kinetic beam energy	4.4 MeV
Relative energy spread $\delta\gamma/\gamma$, FW50	1.5×10^{-5}

large magnification ratio maintaining a reasonable total length for the entire microscope.

A. Permanent magnet quadrupole as the lens

The solenoidal coil is the most commonly used type of electron lens due to the simple axially symmetric geometry. The focal length of a solenoid is $f = [K_s \sin(K_s L)]^{-1}$, where L is the effective magnetic length, $K_s = e_0 B_0 / (2\gamma \beta m_0 c_0)$, and B_0 is the field strength. For $\gamma = 10$ electrons, assuming $B_0 = 2.2$ T, we have $f = 1.6$ cm for $L = 2.5$ cm. Such lenses are technically feasible but are very heavy and bulky. For example, the objective lens of the 3-MV electron microscope at Osaka University is >1 tons in weight [57]. The field strength of a normal conducting solenoid can hardly be further increased due to the saturation of pole-piece materials. Superconducting solenoids are a viable technology to reach higher field amplitudes, as in large bore devices fields as high as 40 T have been demonstrated [58]. Nevertheless, these magnets have long effective lengths, and significant research and development is required in order to adapt this technology for use in building low-aberration strong lenses for MeV TEMs.

An alternative approach is to use quadrupole magnets. Compared with solenoidal lenses, quadrupoles are much more effective in focusing high-energy electrons, since the magnetic field is perpendicular to the beam path and the magnetic field component of Lorentz force is

maximized. The focal length of a quadrupole magnet can also be expressed as $f = [K_q \sin(K_q L)]^{-1}$. Here $K_q = \sqrt{e_0 G/\beta\gamma m_0 c_0}$, where $G = B_0/a$ is the field gradient and B_0 and a are the tip magnetic field strength and radius of the pole piece, respectively.

Among various kinds of quadrupoles, the permanent magnet quadrupole (PMQ) is a convenient, strong, and compact type, widely used for proton or heavy ion beams or for high-energy electrons anywhere ultrastrong focusing is demanded [59–62]. The field gradient can be as high as a few hundred T/m with a typical permanent magnetic material of $B_0 = 1.2$–1.4 T. The effective length is typically set by its physical thickness and the aperture diameter $2a$, which can be as short as a few millimeters. In what follows, we will consider an electron column design based on PMQs, but most of the considerations can be extended to designs utilizing different kind of quadrupoles.

For example, a recent exciting advancement in the nanofabrication technique has made possible the development of μ magnets, i.e., electromagnets with submillimeter dimensions [63]. For these devices, the pole pieces are shaped and deposited by nanofabrication techniques with submicrometer accuracy, and the current flows in nano-printed electric stripes. The advantages are that the apertures can be very small, hence gradient very high (up to 3000 T/m), and that the focusing strength can be tuned—in contrast to PMQs—simply by adjusting the current in the coils. This technology can also be extended to obtain different magnetic configurations (sextupoles, octupoles, etc.) and has the potential for a revolutionary miniaturization of electron optical elements.

Now we discuss our strategy in the design of the electron column. Quadrupole magnets focus the beam in one transverse plane and defocus in the other. At least three PMQs are required to simultaneously fulfill the requirements of imaging in both the x and y planes and with equal magnifications. In the linear optics transfer matrix formalism, these requirements can be mathematically expressed as $R_{12} = 0$, $R_{34} = 0$, and $R_{11} = R_{33}$. For the initial optimization we use a hard-edge model with parameters listed in Table III derived from RADIA magnetostatic simulations [64] using permanent magnetic material with residual magnetization $B_0 = 1.40$ T and an aperture diameter of 2.0 mm. Since the strength of each PMQ is not tunable, the optical properties of the entire triplet are controlled by

changing the interspacing between PMQs. In Table III, we report the positions of the elements in the triplet that provide equal magnification imaging in the x and y planes. The object plane and image plane are located at $z_o = 0$ and $z_i = 0.2$ m, respectively.

The transfer matrix between z_o and z_i is

$$R = \begin{pmatrix} -11.8 & R_{12} & 0 & 0 \\ -57.0 & -8.46 \times 10^{-2} & 0 & 0 \\ 0 & 0 & -11.8 & R_{34} \\ 0 & 0 & -73.8 & -8.46 \times 10^{-2} \end{pmatrix}. \tag{4}$$

The R_{12} and R_{34} terms can be infinitely small in ideal numerical solutions. With state-of-the-art piezo-based high-precision control of the PMQ positions at a few-nanometer level, these two terms can be made $< 1 \times 10^{-6}$ m/rad. More detailed tolerance studies should include the tilt, rotation, and strength error of the PMQs.

It is possible to calculate the aberrations of the optical system by looking at the higher-order terms in the transfer matrix. In particular, we find $C_{c,x} \equiv T_{126}/M = 14$ mm, $C_{s,x} \equiv U_{1222}/M = 8.6$ mm, $C_{c,y} \equiv T_{346}/M = 48$ mm, and $C_{s,y} \equiv U_{3444}/M = 95$ mm, where $M \equiv -R_{11} = -R_{33} = 11.8$ is the magnification. These values can be obtained directly from the output file of a high-order transport code such as COSY INFINITY [65] and have been verified by fitting the results of single-particle GPT-tracking simulations.

In Fig. 4, we show how the relative beam energy spread $\delta\gamma/\gamma$ and the collection semiangle β affect the image size (beam spot size on the image plane) of a point source. The image size value is converted back to the object plane by dividing the magnification. These results indicate that the blur in the image induced by aberrations can be kept below
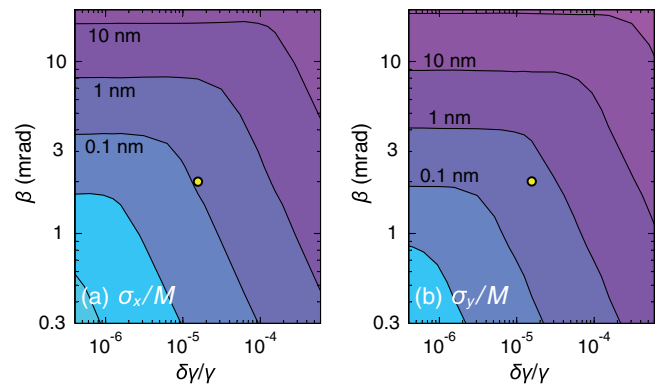
TABLE III. Parameters of the PMQs for a single triplet imaging stage.

Name	Thickness	Gradient	Position
Q_1	6 mm	506.9 T/m	6.747 02 mm
Q_2	6 mm	−506.9 T/m	14.922 82 mm
Q_3	3 mm	537.4 T/m	21.674 76 mm

FIG. 4. GPT-tracking results of the dependence of the FW50 image size (a) σ_x/M and (b) σ_y/M of a point source, on its FW50 relative energy spread $\delta\gamma/\gamma$ (Gaussian distribution) and the objective collection semiangle β (uniform angular distribution).

1 nm if we limit the collection semiangle to 2 mrad and the energy spread at a low 10^{-5} level, in agreement with the back-of-the-envelope estimates discussed in Sec. II. For larger values, chromatic and spherical aberrations quickly increase the beam size and degrade the imaging performances. The differences in the x and y planes are due to the order of the quadrupole orientation in the triplet. By rotating 90° all of the PMQs, we reverse the horizontal and vertical aberration coefficients.

Practical PMQs have fringe fields extending beyond their physical boundaries and might have higher-order multipole components (for example, an octupole component) other than the ideal quadrupole moment. These effects may cause notably different aberrations compared to those predicted based on the ideal hard-edge model. To evaluate these effects, we performed GPT tracking using fully three-dimensional (3D) field maps of PMQs. The 3D PMQ field maps are generated by using the RADIA model and imported into GPT. The physical model of the PMQ, including cubic permanent magnet blocks, soft iron yoke, and parabolic-shape pole pieces, is shown in Fig. 5, together with the calculated on-axis focusing gradient.

Compared with the hard-edge model, 3D field map results show a reduced magnification, from 11.8 times to 11.5 times, due to the overlap of the fringe fields and hence partial cancellation of the focusing strengths of adjacent PMQs which have opposite polarizations. By fitting the GPT particle-tracking results, we also obtain the aberration coefficients. Chromatic aberrations in both the x and y planes are only increased by 10% compared with the hard-edge model. However, spherical aberrations are larger by a factor of 5–6 due to the residual octupole component in the field map. In Fig. 6(b), we show the image disk of a point source with the collection angle set equal to the beam divergence listed in Table III. The eightfold cross feature related to the octupole field component in 3D field maps is clearly visible. The FW50 disk size referred back to the object plane is still $\lesssim 1$ nm, since a large fraction of the electrons is still concentrated in the bright central spot.
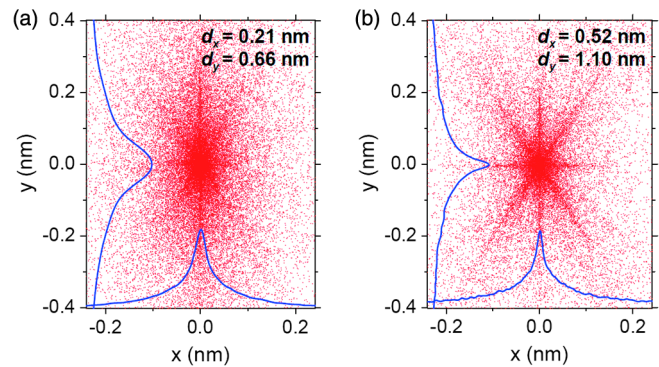
FIG. 6. Image disk profiles of a point source modeled by using (a) the hard-edge ideal quadrupole models and (b) the 3D field map from RADIA. The collection semiangle is 2 mrad, and FW50 beam energy spread is 1.5×10^{-5}. Transverse dimensions have been referred back to the object plane.

Dark field imaging using only electrons scattered to larger angles could also be considered. The disk size stays <5 nm with the collection semiangle increased to 3 mrad. Further reduction of the C_s by optimizing the pole-tip shapes, and whether it is possible to decrease the C_s to even below the ideal hard-edge quadrupoles values, i.e., building a C_s-corrected PMQ triplet, are interesting topics for future studies.

The image size of a point source here is not necessarily the spatial resolution of the microscope. Shot noise due to finite electron flux and e-e interactions within the beam, which will be discussed in the next section, may be larger limiting factors to the spatial resolution. Finally, it is worth noting that the wavelike property of electrons is not included in these calculations. For $\gamma = 10$ electrons (de Broglie wavelength 0.25 pm) and a few-mrad collection angle, the diffraction-limited resolution is on the order of 1 Å and thus has negligible effect on the spatial resolution of the instrument.

In our conceptual design, the complete imaging column includes two more stages—an intermediate stage and a projector stage—after the objective triplet lens. The intermediate stage uses the same PMQ triplet as the objective lens and magnifies 30.7 times in 0.5 m. PMQs in the projector stage need to use larger apertures to accommodate the magnified beam spot size and hence have a reduced focusing gradient. The projector stage magnifies 28.4 times in 1 m. The magnification of the entire column is $11.5 \times 30.7 \times 28.4 = 1.0 \times 10^4$ times. A 10-nm area and the 2-μm illuminated region of the sample will be imaged to 100 μm and 2 cm at the image plane, respectively, comfortably accommodated by the spatial resolution and field of view of the state-of-the-art high-efficiency detector for MeV electrons [66].
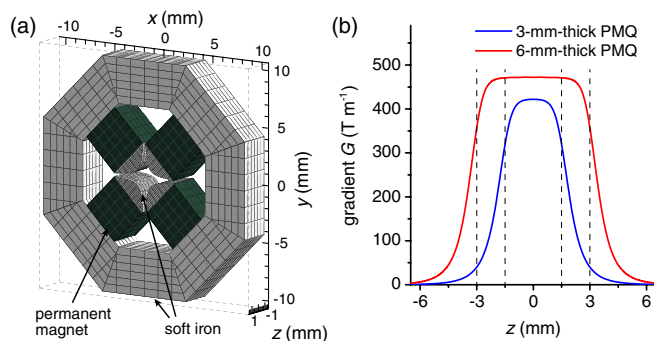

FIG. 5. (a) RADIA model of a 3-mm-thick PMQ magnet and (b) the calculated on-axis focusing gradient of a 3-mm and a 6-mm PMQ. Dashed lines indicate the physical boundaries of the 3- and 6-mm-thick PMQs.

B. Simulation of the imaging process

We then simulate the image formation process of a test target through the column under the optical setting we

discussed above. The test target consists of four groups of horizontal and vertical line pairs similar to those in the widely used USAF 1951 target. The four groups have a linewidth and spacing of 15, 10, 5, and 2.5 nm, respectively. The bright-field imaging mode is considered here. We assume that the electrons hitting the bars are unscattered and thus have a transverse momentum spread $\gamma\sigma_\theta = 9.5$ mrad, the same as the illumination beam listed in Table III. Electrons hitting other regions of the test target are assumed to be scattered to 5 times the illumination angle. An aperture is set up at 3 mm after the sample, and the aperture size allows all the unscattered electrons to go through while approximately 96% of scattered electrons are blocked. The beam energy spread is assumed to stay at the same level, since the energy loss in most samples will be a very small fraction of the MeV kinetic energy.

In Fig. 7, we show the simulated images for three illumination flux levels of (a) $F = 200e/(10 \text{ nm})^2$, (b) $50e/(10\text{nm})^2$, and (c) $F = 12.5e/(10\text{nm})^2$. Otherwise identical beam parameters are used for the three images. The relative intensity fluctuation of a feature in the image is $1/l\sqrt{F}$, where $l \times l$ is the feature size and F is the beam flux. As either the beam flux or feature size becomes smaller, the increased intensity fluctuation gets close to the contrast in the image, which is close to unity for the test

FIG. 7. Simulated electron beam images of the test target under beam illumination flux levels of (a) $200e/(10 \text{ nm})^2$, (b) $50e/(10 \text{ nm})^2$, and (c) $12.5e/(10 \text{ nm})^2$.

target. The visibility of the features in Fig. 7 can be used to estimate the limit on the spatial resolution.

V. ELECTRON-ELECTRON INTERACTIONS

In the previous section discussing the design of the electron optical column, e-e interactions are not taken into account; hence, the size of the image disk of a point source is completely determined by the collection angle, beam energy spread, and the intrinsic aberrations of the electron lenses. In reality, e-e interactions may distort or even wash out the information of the sample imprinted in the beam phase space as the beam propagates from the sample to the detector plane. In this section, we evaluate these effects.

e-e interactions in a beam can be represented by the sum of the smooth space-charge forces and the stochastic scattering resulting from pairwise discrete particle interactions [67]. In order to evaluate the smooth space-charge effects, the electron beam can be treated as a non-neutral plasma "fluid" with continuous charge density distribution. The electric and magnetic fields in this case can be calculated by integration over the entire charge density distribution and are also smooth functions in space and time. The stochastic scattering term is due to collisional events when the motion of a particle is primarily affected by one or a few of its nearest neighbours rather than the collective field of the entire beam.

In principle, both components of e-e interactions are inherently included in full-scale (i.e., one macroparticle in a simulation for one real electron) particle tracking using the pairwise interaction model and could be precisely modeled by taking advantage of recent remarkable advances in scientific computing. Nevertheless, it still requires a significant amount of computation resources and time to track through the microscope column a beam with 10^7 electrons even for a single run. For example, a single run with only 10^4 particles requires approximately 50 hour cores. Furthermore, multiple runs are necessary to reveal the scaling with relevant parameters and guide the design and optimization of the microscope.

Unfortunately, it is also not possible to simply scale [68] the simulation, that is, only simulate a small transverse portion of the beam which has the same charge density evolution as the full beam, to significantly reduce simulation time. To illustrate this point, we show in Fig. 8 the beam spot size and charge density in the first stage of the column for the full beam (2-μm diameter) and a scaled beam with 100-nm-diameter spot size. The two beams have the same initial current density, energy spread, and divergence.

The mesh-based SPACECHARGE3DMESH algorithm in GPT is suitable to model the transverse profile evolution of the full beam [67]. For the scaled 100-nm beam the SPACECHARGE3DMESH algorithm and a full-scale simulation using the pairwise SPACECHARGE3D algorithm (which is now feasible due to the reduced number of particles) yield almost identical (within 2%) results. The charge
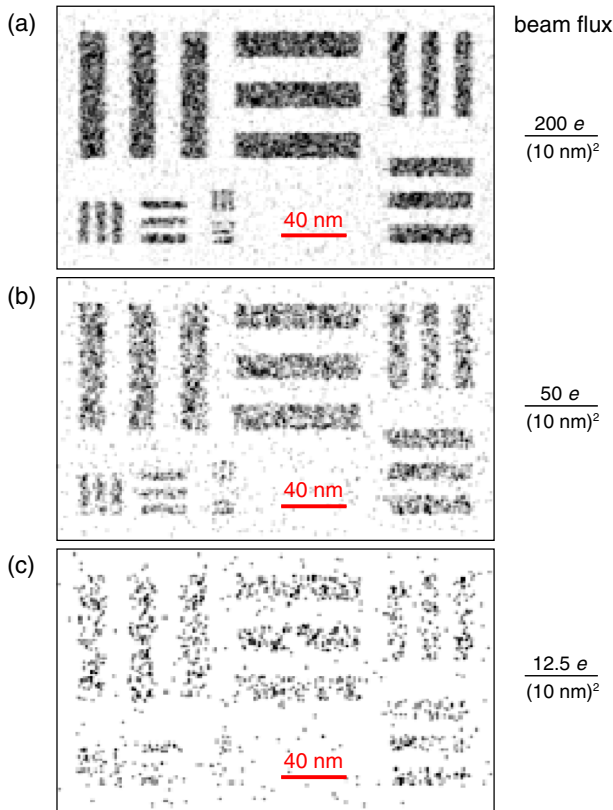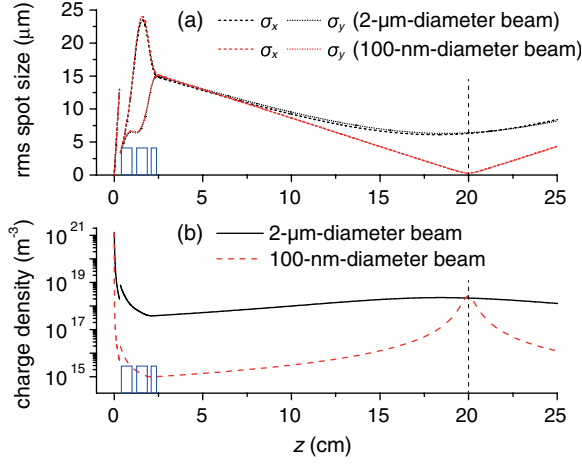
FIG. 8. (a) rms spot size σ_x and σ_y and (b) charge density evolution in the first stage of the column of the full beam (2-μm initial diameter, black line) and a transversely scaled beam (100-nm initial diameter, red line). The blue rectangles represent PMQ positions of the objective lens.

densities of the two beams are exactly the same at the sample plane ($z_o = 0$). In a large portion of the column, the beam spot size is determined by initial divergence, which is the same for both beams. For the scaled beam its charge density is much smaller, and thus the effects of e-e interactions are severely underestimated, roughly by a factor of g_t^2 with g_t being the transverse scaling factor $g_t = 2~\mu$m$/100$ nm $= 20$. The charge densities for the two cases become roughly equivalent again only close to the image plane ($z_i = 20$ cm), where the transverse profiles of both beams are roughly magnified by the same amount. In fact, space-charge effects have a notable effect in the full beam case, generate a shift of the image plane, and are responsible for the small difference in charge density close to z_i.

These considerations lead us to the development of alternative new strategies to calculate the effects of e-e interactions in the column. We discuss how the smooth space-charge defocusing forces, mostly the nonlinear part, affect the imaging condition in Sec. V A. The effects of the stochastic scattering are considered in Sec. V B.

A. Smooth space-charge effects

The strategy to calculate the effects of smooth space-charge forces can be summarized in three steps. (i) Calculate the evolution of the density profile of the full beam in the column. This calculation can be done by using a relatively small number of macroparticles (approximately 10^4, compared to approximately 10^7 in a full-scale simulation) using a mesh-based space-charge algorithm. (ii) Calculate the smooth space-charge field map within the beam, based on the charge density evolution, at any position in the column. (iii) Track the motion of each individual electron in the

smooth space-charge field map, superimposed with the PMQ fields.

In its rest frame, the beam has an elongated shape (beam aspect ratio $A = \gamma\sigma_z/\sigma_{x,y} \gg 1$), and thus the space-charge electric fields are predominately transverse. The magnitudes of the transverse electric fields $E_{x,y}$ scale with the beam current density. For example, for a long, transversely uniform elliptical beam, $E_{x,y}$ at a point (x, y) can be written as

$$E_{x,y} = \frac{I(r_x, r_y)}{\pi\epsilon_0 c_0 \beta} \frac{x(y)}{r_{x,y}(r_x + r_y)}, \quad (5)$$

where $r_{x,y}$ are the semiaxes of the smaller ellipse passing by point (x, y) and $I(r_x, r_y)$ is the enclosed beam current. The ratio $r_x/r_y = \sigma_x/\sigma_y$, where σ_x and σ_y are the rms spot sizes of the full beam. Equation (5) is strictly valid only for a uniform density beam but can be used as a first approximation to describe the fields of any elliptical charge distribution [69]. Electric repulsion forces are partially canceled by magnetic attraction, and thus the total space-charge forces acting on the particles can be represented by $E_{x,y}^s = E_{x,y}/\gamma^2$. We fit $I(r_x, r_y)$ by using polynomial functions [70] (up to tenth order). A smooth space-charge field map is then calculated based on the smooth polynomial representation of I using Eq. (5) and imported into GPT as an external three-dimensional electric field map. Particles are tracked in the superimposed space-charge field and PMQ field without turning on any e-e interactions in GPT. In Fig. 9(a), we compare the spot size σ_x of the full beam simulated by using this technique with that obtained directly by using the SPACECHARGE3DMESH method. The good agreement between the two curves provides evidence of the validity of this technique.

It is then possible to track particles from a point source at high precision to evaluate the aberrations associated with the smooth space-charge field. The black dotted line in Fig. 9(b) shows the FW50 spot size of the beam from a point source under only the PMQ field. When a smooth space-charge field map of the full beam is included, the position of the new "image plane" is significantly shifted downstream, consistent with our understanding that space-charge forces are defocusing. Furthermore, the size of the "image" is significantly larger due to the strong aberration introduced by the space-charge field.

If the transverse beam profile is uniform, i.e., the fitting result of $I(r_x, r_y)$ contains only second-order terms, the associated space-charge forces will be perfectly linear functions of transverse positions minimizing the aberration. This result is confirmed in simulation. When only the linear part of the space-charge field is included in particle tracking, the image plane is shifted but the size of the image disk is only slightly increased, as shown by the dark cyan dash-dotted curve in Fig. 9(b). After a smooth space-charge field map is included, the PMQ focusing needs to be adjusted (strengthened) to image again at z_i, and hence the
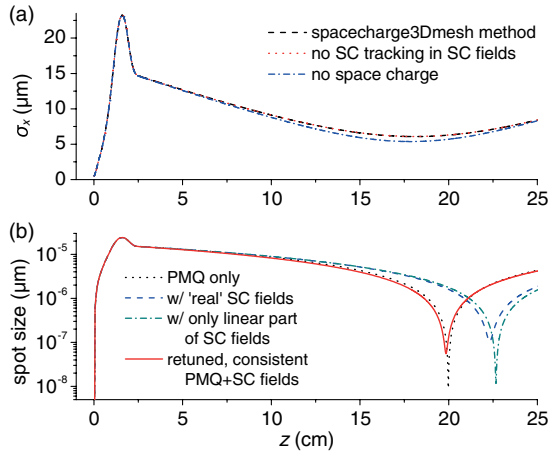
FIG. 9. (a) Comparison of the spot size obtained (black dashed line) directly by using the SPACECHARGE3DMESH method and (red dotted line) the one using superposed PMQ and space-charge field map without turning on any e-e effects in GPT. The result (blue dash-dotted line) with only the PMQ field is also shown. (b) Spot size evolution of a point source (black dotted line) with only the PMQ field tuned at imaging at $z_i = 20$ cm, (blue dashed line) after including the smooth space-charge field, and (cyan dash-dotted line) with only the linear component of the smooth space-charge field. (Red solid line) The PMQ triplet is retuned to image at z_i again with the new space-charge field calculated under the new PMQ setting.

space-charge field map needs to be recalculated. A few iterations allow imaging at z_i in a self-consistent way with a new PMQ setting and the space-charge field calculated under the same new PMQ setting. The red solid line in Fig. 9 shows the spot size under the new optical and space-charge field settings.

Linear space-charge defocusing forces do not notably degrade the image disk, but the integrated space-charge defocusing effect has to be smaller than PMQ focusing to ensure the formation of crossover and imaging. The field gradients of the linear part in the space-charge field $E_{x(y)}^{s,\mathrm{lin}}/x(y)$ are shown in Fig. 10(a). For example, a 10^4 MV/m^2 defocusing field gradient needs to be counterbalanced by a 33 T/m quadrupole field or 0.26-T solenoid field.

Nonlinear components in space-charge fields are directly related to the nonuniform density profile of the beam. The lowest-order nonlinear component of the density distribution scales as x^4 and y^4, and the associated space-charge forces have x^3 and y^3 dependence, contributing to particle motion as dynamic spherical aberrations. Higher-order nonlinear components in density and field distributions also exist but at smaller magnitudes.

As discussed in Sec. III, the beam distribution at the sample is approximately uniform both in density and in angle, so at least initially the space-charge field is mostly linear. The nonuniformity in density distribution mainly originates from the evolution of the beam initial state along
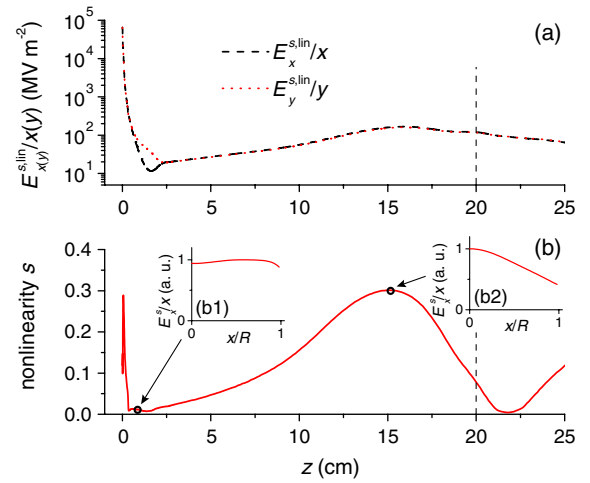

FIG. 10. (a) Field gradients of the linear part in the space-charge field. (b) Nonlinearity s of the space-charge field. The field gradient E_x^s/x at two positions where nonlinearity is (b1) low and (b2) high is shown.

the column. At each z position in the column, the transverse coordinate of a particle can be written (at first order) as the sum of $R_{11}x$, related to its initial position and $R_{12}x'$ proportional to its initial divergence. Whenever one of these terms dominates over the other one the beam distribution is uniform and the resulting space-charge field is linear, but when the two terms are comparable the beam transverse profile is given by the convolution of the initial position and angle distributions and becomes strongly nonuniform with a decreasing density at its edge.

We quantify the nonlinearity by using a parameter $s = \int s(x)dx/\int dx$, where $s(x) = |I^{\mathrm{full}}(x) - I^{\mathrm{2nd}}(x)|/|I^{\mathrm{full}}(x)|$ and $I^{\mathrm{full}}(x)$ and $I^{\mathrm{2nd}}(x)$ are the complete polynomial fitting results of the beam shape and only the second-order (uniform) component, respectively. The s value in the first stage of the column is shown in Fig. 10(b). The beam density is only roughly uniform close to the object and image planes and characterized by strong nonlinear components at other positions.

The effects of nonlinear space-charge forces can be quantified by using equivalent spherical aberration coefficients C_3^s and C_5^s, related to the third- and fifth-order space-charge field, respectively. These coefficients can be extracted by fitting GPT particle-tracking results for the position on the image plane of a single particle with a varying initial angle at the object plane. For example, with the current design we have $C_{x,5}^s = -2.5 \times 10^6$ m, $C_{x,3}^s = 2.4$ m and $C_{y,5}^s = -4.5 \times 10^6$ m, $C_{y,3}^s = 5.0$ m. The magnitudes of these aberration coefficients are determined by the transverse profile (relative importance of nonlinear components) and the average current density of the beam. It might be possible to minimize these coefficients by varying the PMQ focal length, stage length, beam spot size, and divergence at the sample, as well as the
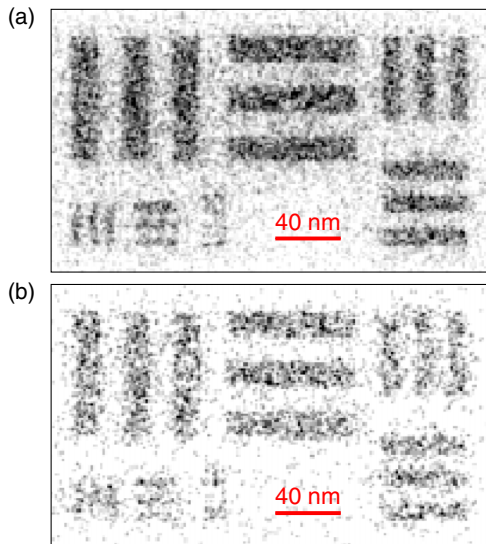
FIG. 11. Simulated image of the test target for (a) $200e/(10\text{ nm})^2$ and (b) $50e/(10\text{ nm})^2$ illumination flux, with smooth space-charge effects taken into account.

imaging mode (bright-field or dark-field). An intriguing research opportunity is to explore octupole- and dodeca-pole-based correction modules to minimize the smooth space-charge spherical aberrations in an independent and flexible way.

Finally, we apply the above computation scheme to visualize the image of the test target. In Fig. 11, we show the images for (a) $200e/(10\text{ nm})^2$ and (b) $50e/(10\text{ nm})^2$ illumination flux at the end of the first stage with dimensions converted back to the object plane. Space-charge aberration coefficients in the second stage are up to 10 times larger than those of the first stage. But due to the M times smaller divergence at the entrance to the second stage (hence M^3 times smaller image disk size scaling) and M times larger "object" size, smooth space-charge effects have a negligible impact on image quality in the second and following stages of the column. As shown in Fig. 11, 10-nm line pairs can be clearly distinguished in both the x and y planes. The visibility of 5-nm-wide line pairs is notably degraded compared to the result when smooth space-charge effects are not included. We note that the smooth space-charge aberration is proportional to the beam current density and the shot-noise-limited resolution is inversely proportional to the square root of beam flux. Thus, for a given bunch length, there exists an optimum condition for the spatial resolution which is given by the beam current for which the contributions from smooth space-charge effects and shot noise are comparable.

B. Stochastic scattering effects

Stochastic scattering between close-by particles can lead to an increase in the beam divergence along the column which results in a degradation of the image resolution.

First-principle pairwise e-e interaction algorithms need to be used to precisely model this effect. A longitudinally scaled simulation, i.e., simulating a full-transverse size but a thin longitudinal slice of the beam, can correctly predict the e-e interaction effects if the aspect ratio of the slice stays $\gg 1$ and the space-charge forces remain predominantly transverse. By scaling down the bunch length by a large factor $g_l = \tau_{\text{full}}/\tau_{\text{slice}}$ (for example, up to 100), the computation time becomes manageable even using the pairwise algorithm, but the beam flux on the screen will be much smaller than reality by a factor of g_l, preventing us from the possibility to visualize the image due to shot-noise considerations. τ_{full} and τ_{slice} are the length of the full beam and the slice, respectively. To this end, we adopt the "image-disk convolution" approach to model the image and evaluate spatial resolution under e-e interactions as described below.

If there is an ideal imaging from the object plane to the image plane, then $w \equiv -Mx_o - x_i$ will be zero for each particle, where M is the magnification and the minus sign before M is due to the fact that the image is reversed. In reality, aberrations due to both PMQs and e-e interactions spread w to a disk of finite size on the image plane. The shape of the w disk should quantitatively agree with the image disk of a point source, as the two distributions essentially both describe how a point is imaged to a finite size due to the presence of aberrations. This agreement is confirmed, as shown in Fig. 12(a), where we show the profiles of the image of a point source (red solid line) and the w disk of a full-transverse-size (2-μm-diameter) beam in good agreement with each other. These two profiles are simulated by using the smooth space-charge fields discussed in Sec. VA. The $200e/(10\text{ nm})^2$ illumination flux and 2-mrad collection semiangle are assumed. Roughly 25% of particles go through the objective aperture located
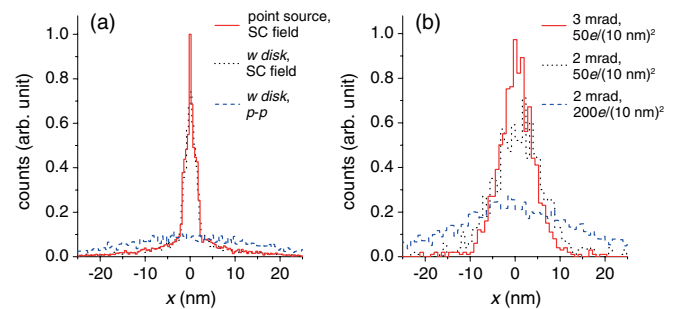

FIG. 12. (a) Histogram of the image of a point source (red solid line) and w disk of a full-transverse-size beam (black dotted line) tracked in the smooth space-charge field, together with the w disk of a full-transverse-size beam tracked by using the first-principle pairwise e-e interaction model (blue dashed line). (b) w disk of a full-transverse-size beam tracked by using the first-principle pairwise e-e interaction model with divergence and illumination flux of (red solid line) 3 mrad, $50e/(10\text{ nm})^2$, (black dotted line) 2 mrad, $50e/(10\text{ nm})^2$, and (blue dashed line) 2 mrad, $200e/(10\text{ nm})^2$.

at 3 mm. Finally, by convolving the *w*-disk or image-disk profile with the ideal image of the test target, we can compute the image at the detector plane.

A thin longitudinal slice of the full beam ($g_l = 100$) is simulated in GPT under PMQ fields using the first-principle pairwise *e-e* algorithm (SPACECHARGE3D method). The simulation in principle includes the effects of both stochastic scattering and smooth space charge. The number of particles used in the simulation is equal to the number of electrons in the slice. Random, instead of Hammersley sequence, distributions in initial positions and angles are used. The *e-e* interactions shift the position of the image plane. The minimal FW50 size of the *w* disk is actually a good indication to find both the position of the image plane and the magnification value. The result (blue dotted line) is shown in Fig. 12(a). The same initial beam conditions as those for the other two curves are used. The result shows that stochastic scattering introduces a large spread of the image disk which notably degrades the spatial resolution.

A straightforward approach to reduce the effects of stochastic scattering is to decrease the beam illumination flux, e.g., to the $50e/(10 \text{ nm})^2$ level, which still allows good visibility of 10-nm full width line pairs. As shown in

FIG. 13.   Images of the test target simulated with first-principle pairwise *e-e* interaction model, for a beam divergence and illumination flux of (a) 2 mrad, $200e/(10 \text{ nm})^2$, (b) 2 mrad, $50e/(10 \text{ nm})^2$, and (c) 3 mrad, $50e/(10 \text{ nm})^2$.

Fig. 12(b), a 4 times reduction in beam flux leads to roughly a 2 times decrease in the FW50 size of the *w* disk. We can further decrease the size of the *w* disk by increasing beam divergence (assumed matched by the collection semiangle for the bright-field imaging mode), which helps to reduce the charge density after the sample, until the geometric aberration of the PMQ triplet prevents the image disk from becoming smaller. As an example, we show in Fig. 12(b) that, by increasing the beam divergence from 2 to 3 mrad, the FW50 *w*-disk size is reduced from 7.8 to 5.4 nm. The convolutions of the *w* disks with the ideal image of the test target are displayed in Fig. 13. The images show the possibility to resolve the 10-nm full width line pairs. Using lenses with smaller spherical aberrations which accept larger beam divergence (collection angle) and/or a dark-field imaging mode could provide further improvements.

VI. SUMMARY

In conclusion, we analyze various components of a MeV-energy time-resolved TEM driven by an rf photoinjector. Innovations in the source design include a higher accelerating field at photoemission and taking advantage of the cigar regime of operation of rf photoguns. A high-frequency rf cavity is proposed to compensate the beam energy spread and minimize the effects of the chromatic aberration. A quadrupole-based imaging system is discussed and analyzed with the help of particle-tracking simulations. The effects of *e-e* interactions, including smooth space-charge forces and stochastic scattering, on the spatial resolution are studied in detail with strategies. The final system shows the feasibility of taking single-shot images of samples with 10-ps temporal resolution and 10-nm spatial resolution. This instrument can be useful in the study of materials under extreme conditions, such as the response of materials to laser-induced intense pressure and temperature stimuli. Imaging the motion of dislocations under extreme pressures, which is currently possible only at XFELs in diffraction mode [71], is one of the possible applications of this device.

By extending the reach and flexibility of the instrument, the same device can be operated to cover a wider range of spatiotemporal resolution in single-shot mode. For example, one can employ a properly shaped laser pulse train to generate a microsecond-long (naturally matched with the typical rf pulse width for an *S*-band photogun) macro-electron pulse, containing a few thousand identical micro-electron pulses. The train of micropulses, each 10 ps long and spaced by the rf cycle (350 ps for 2856 MHz), has the same 4D transverse brightness of the single pulse discussed earlier in the paper used for 10-nm–10-ps imaging, but due to the fact that each micropulse contains a few thousand times lower charge a much better spatial resolution can be obtained. The angstrom-microsecond resolution capability
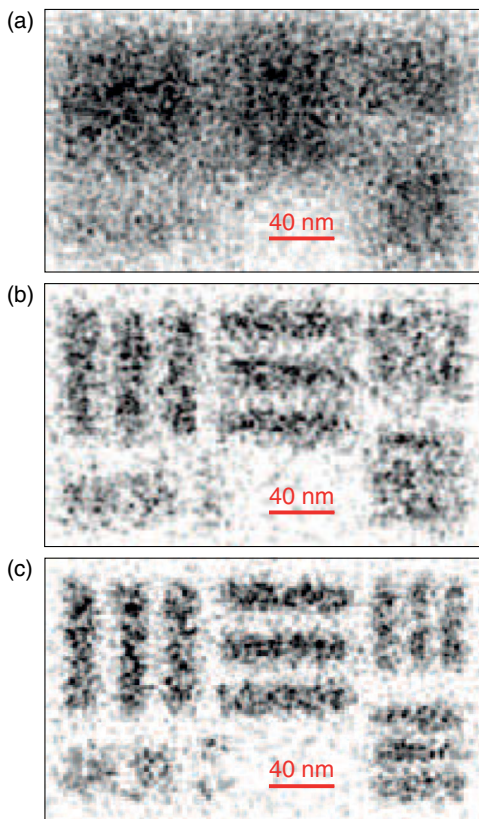
opens up many new research opportunities in mesoscopic materials and biology.

Furthermore, the same device can also be used in the stroboscopic mode with even shorter pulse lengths. Thanks to the improvement in beam brightness due to the relativistic electron source, 10^2–10^3 or more electrons per pulse can be used for atomic scale imaging with 100-fs temporal resolution. This mode can run at the kilohertz repetition rate and thus offers a similar beam current and exposure time as the single-electron keV UEM but allows much higher laser fluence for each pump event before sample damage induced by accumulated heat deposition. It is possible to further improve the temporal resolution down to the 10-fs level by introducing an rf bunching cavity [66,72–74]. Emergent properties of quantum materials following ultrafast photonic excitation can be observed by using this device with spatiotemporal resolution on fundamental atomic scales.

ACKNOWLEDGMENTS

[1] D. B. Williams and C. B. Carter, *Transmission Electron Microscopy: A Textbook for Materials Science*, 2nd ed. (Springer, New York, 2009).

[2] L. Reimer and H. Kohl, *Transmission Electron Microscopy: Physics of Image Formation*, 5th ed. (Springer, New York, 2008).

[3] J. C. H. Spence, *High-Resolution Electron Microscopy*, 4th ed. (Oxford University Press, New York, 2013).

[4] M. Haider, S. Uhlemann, E. Schwan, H. Rose, B. Kabius, and K. Urban, Electron microscopy image enhanced, Nature (London) **392,** 768 (1998).

[5] P. E. Batson, N. Dellby, and O. L. Krivanek, Sub-ångstrom resolution using aberration corrected electron optics, Nature (London) **418,** 617 (2002).

[6] W. E. King, G. H. Campbell, A. Frank, B. Reed, J. F. Schmerge, B. J. Siwick, B. C. Stuart, and P. M. Weber, Ultrafast electron microscopy in materials science, biology, and chemistry, J. Appl. Phys. **97,** 111101 (2005).

[7] *Future Science Needs and Opportunities for Electron Scattering: Next-Generation Instrumentation and Beyond*, Report of the U.S. Department of Energy Basic Energy Sciences Workshop on Electron Scattering for Materials Characterization (U.S. Department of Energy, Gaithersburg, MD, 2007).

[8] F. Carbone, P. Musumeci, O. J. Luiten, and C. Hebert, A perspective on novel sources of ultrashort electron and x-ray pulses, Chem. Phys. **392,** 1 (2012).

[9] O. Bostanjoglo, High-speed electron microscopy, Adv. Imaging Electron Phys. **121,** 1 (2002).

[10] H. Domer and O. Bostanjoglo, High-speed transmission electron microscope, Rev. Sci. Instrum. **74,** 4369 (2003).

[11] T. LaGrange, M. R. Armstrong, K. Boyden, C. G. Brown, G. H. Campbell, J. D. Colvin, W. J. DeHope, A. M. Frank, D. J. Gibson, F. V. Hartemann, J. S. Kim, W. E. King, B. J. Pyke, B. W. Reed, M. D. Shirk, R. M. Shuttlesworth, B. C. Stuart, B. R. Torralva, and N. D. Browning, Single-shot dynamic transmission electron microscopy, Appl. Phys. Lett. **89,** 044105 (2006).

[12] J. S. Kim, T. LaGrange, B. W. Reed, M. L. Taheri, M. R. Armstrong, W. E. King, N. D. Browning, and G. H. Campbell, Imaging of transient structures using nanosecond *in situ* TEM, Science **321,** 1472 (2008).

[13] A. H. Zewail, Four-dimensional electron microscopy, Science **328,** 187 (2010).

[14] A. H. Zewail and J. M. Thomas, *4D Electron Microscopy: Imaging in Space and Time* (Imperial College Press, London, 2010).

[15] L. Piazza, P. Musumeci, O. J. Luiten, and F. Carbone, A proposal for fs-electron microscopy experiments on high-energy excitations in solids, Micron **63,** 40 (2014).

[16] T. Rao and D. H. Dowell, An Engineering Guide To Photoinjectors, arXiv:1403.7539.

[17] R. Akre, D. Dowell, P. Emma, J. Frisch, S. Gilevich, G. Hays, Ph. Hering, R. Iverson, C. Limborg-Deprey, H. Loos, A. Miahnahri, J. Schmerge, J. Turner, J. Welch, W. White, and J. Wu, Commissioning the Linac Coherent Light Source injector, Phys. Rev. ST Accel. Beams **11,** 030703 (2008).

[18] X. J. Wang, Z. Wu, and H. Ihee, in *Proceedings of PAC03* (IEEE, Portland, OR, 2003), WOAC003.

[19] J. B. Hastings, F. M. Rudakov, D. H. Dowell, J. F. Schmerge, J. D. Cardoza, J. M. Castro, S. M. Gierman, H. Loos and P. M. Weber, Ultrafast time-resolved electron diffraction with megavolt electron beams, Appl. Phys. Lett. **89,** 184109 (2006).

[20] P. Musumeci, J. T. Moody, C. M. Scoby, M. S. Gutierrez, and M. Westfall, Laser-induced melting of a single crystal gold sample by time-resolved ultrafast relativistic electron diffraction, Appl. Phys. Lett. **97,** 063502 (2010).

[21] R. K. Li, C. X. Tang, Y. C. Du, W. H. Huang, Q. Du, J. R. Shi, L. X. Yan, and X. J. Wang, Experimental demonstration of high quality MeV ultrafast electron diffraction, Rev. Sci. Instrum. **80,** 083303 (2009).

[22] Y. Murooka, N. Naruse, S. Sakakihara, M. Ishimaru, J. Yang, and K. Tanimura, Transmission-electron diffraction by MeV electron pulses, Appl. Phys. Lett. **98,** 251903 (2011).

[23] P. F. Zhu, H. Berger, J. Cao, J. Geck, Y. Hidaka, R. Kraus, S. Pjerov, Y. Shen, R. I Tobey, Y. Zhu, J. P. Hill, and X. J. Wang, Femtosecond time-resolved MeV electron diffraction, arXiv:1304.5176.

[24] http://regae.desy.de/.

[25] J. Yang, in *Proceedings of the Workshop on Ultrafast Electron Sources for Diffraction and Microscopy Applications, Los Angeles, 2012*, http://pbpl.physics.ucla.edu/UESDM_2012/.

[26] R. K. Li and P. Musumeci, in *Proceedings of the 25th North American Particle Accelerator Conference, Pasadena, 2013*, http://accelconf.web.cern.ch/accelconf/pac2013/talks/thoaa1_talk.pdf.

[27] D. Xiang, F. Fu, J. Zhang, X. Huang, L. Wang, X. Wang, and W. Wan, Accelerator-based single-shot ultrafast transmission electron microscope with picosecond temporal resolution and nanometer spatial resolution, Nucl. Instrum. Methods Phys. Res., Sect. A **759,** 74 (2014).

[28] A. Rose, Television pickup tubes and the problem of vision, Adv. Electron. Electron Phys. **1**, 131 (1948).

[29] G. H. Jansen, Coulomb interactions in particle beams, J. Vac. Sci. Technol. B **6**, 1977 (1988).

[30] G. H. Jansen, *Coulomb Interactions in Particle Beams* (Academic, Waltham, MA, 1990).

[31] B. W. Reed, M. R. Armstrong, N. D. Browning, G. H. Campbell, J. E. Evans, T. LaGrange, and D. J. Masiel, The evolution of ultrafast electron microscope instrumentation, Microsc. Microanal. **15**, 272 (2009).

[32] ICFA Beam Dynamics Newsletter No. 46, edited by M. A. Furman and W. Chou, 2008.

[33] D. Filippetto, P. Musumeci, M. Zolotorev, and G. Stupakov, Maximum current density and beam brightness achievable by laser-driven electron sources, Phys. Rev. ST Accel. Beams **17**, 024201 (2014).

[34] R. F. Egerton, P. Li, and M. Malac, Radiation damage in the TEM and SEM, Micron **35**, 399 (2004).

[35] J. C. H. Spence, U. Weierstall, and H. N. Chapman, X-ray lasers for structural and dynamic biology, Rep. Prog. Phys. **75**, 102601 (2012).

[36] D. H. Dowell and J. F. Schmerge, Quantum efficiency and thermal emittance of metal photocathodes, Phys. Rev. ST Accel. Beams **12**, 074201 (2009).

[37] D. H. Dowell, I. Bazarov, B. Dunham, K. Harkay, C. Hernandez-Garcia, R. Legg, H. Padmore, T. Rao, J. Smedley, and W. Wan, Cathode R&D for future light sources, Nucl. Instrum. Methods Phys. Res., Sect. A **622**, 685 (2010).

[38] R. K. Li, K. G. Roberts, C. M. Scoby, H. To, and P. Musumeci, Nanometer emittance ultralow charge beams from rf photoinjectors, Phys. Rev. ST Accel. Beams **15**, 090702 (2012).

[39] S. Di Mitri and M. Cornacchia, Electron beam brightness in linac drivers for free-electron-lasers, Phys. Rep. **539**, 1 (2014).

[40] I. V. Bazarov, B. M. Dunham, and C. K. Sinclair, Maximum achievable beam brightness from photoinjectors, Phys. Rev. Lett. **102**, 104801 (2009).

[41] B. J. Claessens, S. B. van der Geer, E. J. D. Vredenbregt, and O. J. Luiten, Ultracold electron source, Phys. Rev. Lett. **95**, 164801 (2005).

[42] O. J. Luiten, S. B. van der Geer, M. J. de Loos, F. B. Kiewiet, and M. J. van der Wiel, How to realize uniform three-dimensional ellipsoidal electron bunches, Phys. Rev. Lett. **93**, 094802 (2004).

[43] P. Musumeci, J. T. Moody, R. J. England, J. B. Rosenzweig, and T. Tran, Experimental generation and characterization of uniformly filled ellipsoidal electron-beam distributions, Phys. Rev. Lett. **100**, 244801 (2008).

[44] F. Zhou, A. Brachmann, P. Emma, S. Gilevich, and Z. Huang, Impact of the spatial laser distribution on photocathode gun operation, Phys. Rev. ST Accel. Beams **15**, 090701 (2012).

[45] C. P. Hauri, R. Ganter, F. Le Pimpec, A. Trisorio, C. Ruchert, and H. H. Braun, Intrinsic emittance reduction of an electron beam from metal photocathodes, Phys. Rev. Lett. **104**, 234802 (2010).

[46] X. J. Wang, X. Qiu, and I. Ben-Zvi, Experimental observation of high-brightness microbunching in a photocathode rf electron gun, Phys. Rev. E **54**, R3121(R) (1996).

[47] General Particle Tracer, http://www.pulsar.nl/gpt/.

[48] T. I. Smith, in Proceedings of 1986 Linear Accelerator Conference, Stanford, CA, 1986, Report No. SLAC-R-303, pp. 421–426.

[49] L. Serafini, R. Rivolta, and C. Pagani, Neutralization of the emittance blowup induced by rf time dependent forces in rf guns, Nucl. Instrum. Methods Phys. Res., Sect. A **318**, 301 (1992).

[50] D. H. Dowell, M. Ferrario, T. Kimura, J. Lewellen, C. Limborg, P. Raimondi, J. F. Schmerge, L. Serafini, T. Smith, and L. Young, A two-frequency rf photocathode Gun, Nucl. Instrum. Methods Phys. Res., Sect. A **528**, 316 (2004).

[51] J. Lewellen and J. Noonan, Field-emission cathode gating for rf electron guns, Phys. Rev. ST Accel. Beams **8**, 033502 (2005).

[52] See, for example, J. M. Byrd, L. Doolittle, G. Huang, J. W. Staples, R. Wilcox, J. Arthur, J. Frisch, and W. White, in Proceedings of BIW10, Santa Fe, NM, 2010, MOCNB04, https://accelconf.web.cern.ch/accelconf/BIW2010/papers/mocnb04.pdf.

[53] M. Felber, M. Hoffmann, U. Mavric, H. Schlarb, S. Schulz, and W. Jalmuzna, in Proceedings of IPAC2012, New Orleans, LA, 2012, WEPPD048, http://accelconf.web.cern.ch/accelconf/ipac2012/papers/weppd048.pdf.

[54] F. J. Decker, A. Krasnykh, B. Morris, and M. Nguyen, in Proceedings of the 2012 IEEE International Power Modulator and High Voltage Conference (IPMHVC), San Diego, CA, 2012, pp. 695–699, http://ieeexplore.ieee.org/xpl/articleDetails.jsp?arnumber=6518840.

[55] T. Shintake, T. Inagaki, K. Shirasawa, C. Kondo, and T. Sakurai, in Proceedings of IPAC10, Kyoto, Japan, 2010, WEPD080, https://accelconf.web.cern.ch/accelconf/IPAC10/papers/wepd080.pdf.

[56] B. W. Reed, T. LaGrange, R. M. Shuttlesworth, D. J. Gibson, G. H. Campbell, and N. D. Browning, Solving the accelerator-condenser coupling problem in a nanosecond dynamic transmission electron microscope, Rev. Sci. Instrum. **81**, 053706 (2010).

[57] A. Takaoka, K. Ura, H. Mori, T. Katsuta, I. Matsui, and S. Hayashi, Development of a new 3 MV ultra-high voltage electron microscope at Osaka University, J. Electron Microsc. **46**, 447 (1997).

[58] J. Schwartz, T. Effio, X. Liu, Q. V. Le, A. L. Mbaruku, H. J. Schneider-Muntau, T. Shen, H. Song, U. P. Trociewitz, X. Wang, and H. W. Weijers, High field superconducting solenoids via high temperature superconductorsm, IEEE Trans. Appl. Supercond. **18**, 70 (2008).

[59] K. Halbach, Design of permanent multipole magnets with oriented rare earth cobalt material, Nucl. Instrum. Methods **169**, 1 (1980).

[60] G. J. Ross, G. Garty, G. Randers-Pehrson, and D. J. Brenner, A single-particle/single-cell microbeam based on an isotopic alpha source, Nucl. Instrum. Methods Phys. Res., Sect. B **231**, 207 (2005).

[61] K. Nakamura, T. Sokollik, J. van Tilborg, A. J. Gonsalves, B. Shaw, S. Shiraishi, R. Mittal, S. De Santis, J. M. Byrd, and W. Leemans, Beam transport and monitoring for laser plasma accelerators, AIP Conf. Proc. **1507**, 728 (2012).

[62] J. K. Lim, P. Frigola, G. Travish, J. B. Rosenzweig, S. G. Anderson, W. J. Brown, J. S. Jacob, C. L. Robbins, and

A. M. Tremaine, Adjustable, short focal length permanent-magnet quadrupole based electron beam final focus system, Phys. Rev. ST Accel. Beams **8**, 072401 (2005).

[63] J. Harrison, O. Paydar, Y. Hwang, J. Wu, E. Threlkeld, P. Musumeci, and R. N. Candler, Fabrication process for thick-film micromachined multi-pole electromagnets, J. Microelectromech. Syst. **23**, 505 (2014).

[64] P. Elleaume, O. Chubar, and J. Chavanne, in Proceedings of PAC97, Vancouver, 1997, pp. 3509–3511, http://accelconf .web.cern.ch/accelconf/pac97/papers/pdf/9P027.PDF.

[65] COSY INFINITY, http://www.bt.pa.msu.edu/index_cosy .htm.

[66] R. K. Li, P. Musumeci, H. A. Bender, N. S. Wilcox, and M. Wu, Imaging single electrons to enable the generation of ultrashort beams for single-shot femtosecond relativistic electron diffraction, J. Appl. Phys. **110**, 074512 (2011).

[67] M. Reiser, *Theory and Design of Charged Particle Beams* (Wiley, New York, 2008), pp. 163–170.

[68] Here we refer to the scaling in the transverse direction. Longitudinally scaled simulation will be discussed in Sec. V B.

[69] M. A. Furman, Compact complex expressions for the electric field of two-dimensional elliptical charge distributions, Am. J. Phys. **62**, 1134 (1994).

[70] The polynomial fitting of I uses even-order components (due to middle-plane symmetry) up to tenth order and precisely represents the smooth distribution. For example, when 10^4 macroparticles are used in simulation, the difference of I between direct counting of macroparticles and polynomial fitting is $< 1\%$, on the same magnitude of the macroparticle shot noise.

[71] D. Milathianaki, S. Boutet, G. J. Williams, A. Higginbotham, D. Ratner, A. E. Gleason, M. Messerschmidt, M. M. Seibert, D. C. Swift, P. Hering, J. Robinson, W. E. White, and J. S. Wark, Femtosecond visualization of lattice dynamics in shock-compressed matter, Science **342**, 220 (2013).

[72] T. van Oudheusden, E. F. de Jong, S. B. van der Geer, W. P. E. M. Op t Root, O. J. Luiten, and B. J. Siwick, Electron source concept for single-shot sub-100 fs electron diffraction in the 100 keV range, J. Appl. Phys. **102**, 093501 (2007).

[73] T. van Oudheusden, P. L. E. M. Pasmans, S. B. van der Geer, M. J. de Loos, M. J. van der Wiel, and O. J. Luiten, Compression of subrelativistic space-charge-dominated electron bunches for single-shot femtosecond electron diffraction, Phys. Rev. Lett. **105**, 264801 (2010).

[74] P. Baum, On the physics of ultrashort single-electron pulses for time-resolved microscopy and diffraction, Chem. Phys. **423**, 55 (2013).